

DRAFT VERSION MARCH 8, 2022

Preprint typeset using L<sup>A</sup>T<sub>E</sub>X style AASTeX6 v. 1.0

THE SECOND GALACTIC CENTER BLACK HOLE?; A POSSIBLE DETECTION OF  
IONIZED GAS ORBITING AROUND AN IMBH EMBEDDED IN THE GALACTIC CENTER  
IRS13E COMPLEX

MASATO TSUBOI<sup>1</sup> AND YOSHIMI KITAMURA

Institute of Space and Astronautical Science(ISAS), Japan Aerospace Exploration Agency,

3-1-1 Yoshinodai, Chuo-ku, Sagamihara, Kanagawa 252-5210, Japan

TAKAHIRO TSUTSUMI

National Radio Astronomy Observatory, Socorro, NM 87801-0387, USA

KENTA UEHARA

Department of Astronomy, The University of Tokyo, Bunkyo, Tokyo 113-0033, Japan

MAKOTO MIYOSHI

National Astronomical Observatory of Japan, Mitaka, Tokyo 181-8588, Japan

RYOSUKE MIYAWAKI

College of Arts and Sciences, J.F. Oberlin University, Machida, Tokyo 194-0294, Japan

ATSUSHI MIYAZAKI

Japan Space Forum, Kanda-surugadai, Chiyoda-ku, Tokyo, 101-0062, Japan

(Received; Accepted)

<sup>1</sup>tsuboi@vsop.isas.jaxa.jp

# ABSTRACT

The Galactic Center is the nuclear region of the nearest spiral galaxy, Milky Way, and contains the supermassive black hole with  $M \sim 4 \times 10^6 M_\odot$ , Sagittarius A\* (Sgr A\*). One of basic questions about the Galactic Center is whether Sgr A\* alone exists as a “massive” black hole in the region or not. The IRS13E complex is a very intriguing IR object which contains a large dark mass comparable to the mass of an intermediate mass black hole (IMBH) from the proper motions of the main member stars. However, the existence of the IMBH remains controversial. There are some objections to accepting the existence of the IMBH. In this study, we detected ionized gas with a very large velocity width ( $\Delta v_{\text{FWZI}} \sim 650 \text{ km s}^{-1}$ ) and a very compact size ( $r \sim 400 \text{ AU}$ ) in the complex using ALMA. We also found an extended component connecting with the compact ionized gas. The properties suggest that this would be an ionized gas flow on the Keplerian orbit with high eccentricity. The enclosed mass is estimated to be  $10^4 M_\odot$  by the analysis of the orbit. The mass does not conflict with the upper limit mass of the IMBH around Sgr A\* which is derived by the long-term astrometry with VLBA. In addition, the object probably has an X-ray counterpart. Consequently, a very fascinated possibility is that the detected ionized gas is rotating around an IMBH

embedded in the IRS13E complex.

*Keywords:* accretion, accretion disks—Galaxy: center — stars: formation

## 1. INTRODUCTION

The Galactic Center is the nuclear region of the nearest spiral galaxy, Milky Way, and harbors the Galactic Center black hole, Sagittarius A\* (Sgr A\*) ( $M \sim 4 \times 10^6 M_\odot$ ; e.g. [Ghez et al. 2008](#); [Gillessen et al. 2009](#); [Schödel, Merritt, & Eckart 2009](#); [Boehle et al. 2016](#)). Its environment is unique in the galaxy, in which the region contains several peculiar objects. One of basic questions about the Galactic Center is whether Sgr A\* alone exists as a “massive” black hole ( $\gtrsim 10^4 M_\odot$ ) in the region or not.

The IRS13E complex is a very intriguing IR object in the vicinity of Sgr A\*, which has been identified in the early days of the Galactic Center observations. It is located approximately  $3.5''$  southwest of Sgr A\* in projection ( $r = 0.13$  pc) (e.g. [Genzel et al. 1996](#); [Maillard et al. 2004](#)). The center position of the complex corresponds to the west edge of the Minicavity, which is a hook-like substructure of the Galactic Center Minispiral (GCMS) (e.g. [Lacy et al. 1980](#); [Ekers et al. 1983](#); [Lo & Claussen 1983](#)). The IR observations at the time suggested that the IRS 13E complex contains several massive stars including Wolf-Rayet (WR) and O stars in a diameter of about  $0.5''$ , which have the common direction and similar amplitude of the proper motions (westward proper motion with  $V_{mean} \sim 280 \text{ km}^{-1}$ ) (e.g. [Maillard et al. 2004](#)). This fact indicates that the main members of the complex are physically bound although the complex should be disrupted by the strong tidal force of Sgr A\* (e.g. [Gerhard 2001](#)). One possible speculation was that a dark mass like an intermediate mass black hole (IMBH) in the complex may prevent its tidal disruption (e.g. [Maillard et al. 2004](#)). The mass of the IMBH was estimated to be  $10^4 M_\odot$  from the proper motions of the member stars (e.g. [Maillard et al. 2004](#); [Schödel et al. 2005](#); [Paumard et al. 2006](#)). However, some objections to

the existence of the IMBH emerged from new observations and enviromental evidence (e.g. [Schödel et al. 2005](#); [Fritz et al. 2010](#)). Especially, a recent IR spectroscopic observation indicates that most stars previously detected in the central area of the IRS 13E complex are not massive stars but ionized gas blobs although a few massive stars are certainly identified in the outer area ([Fritz et al. 2010](#)).

We consider that the existence of the IMBH in the IRS13E complex is still an open question. If the IMBH exists, Atacama Large Millimeter/Submillimetr Array (ALMA) can detect the ionized gas accreting onto the IMBH in the IRS13E complex. The accreting ionized gas is expected to have a very large velocity width and a very compact size. We searched such ionized gas with ALMA in order to prove the IMBH hypothesis. Throughout this paper, we adopt 8.0 kpc as the distance to the Galactic center (e.g. [Ghez et al. 2008](#); [Gillessen et al. 2009](#); [Schödel, Merritt,& Eckart 2009](#); [Boehle et al. 2016](#));  $1''$  corresponds to 0.04 pc at the distance.

## 2. OBSERVATION AND DATA REDUCTION

We performed the following observation and analysis. The calibration and imaging of both the data were done by Common Astronomy Software Applications (CASA) ([McMullin et al. 2007](#)).

### 2.1. 340 GHz continuum

We observed the continuum emission of Sgr A\* and the GCMS at 340 GHz as an ALMA Cy.3 program (2015.1.01080.S. PI M.Tsuboi). The observations were performed in three days (23 Apr. 2016, 30/31 Aug. 2016, and 08 Sep. 2016). The observation in April was for detection of extended emission. The field of view in FWHM (FOV) is  $18''$ , which is centered at Sgr A\*:  $\alpha_{\text{ICRS}} = 17^{\text{h}}45^{\text{m}}40^{\text{s}}.04$  and  $\delta_{\text{ICRS}} = -29^{\circ}00'28''.20$ . J1717-3342 was used as a phase calibrator. The flux density scale was determined using Titan and J1733-1304. We used the self-calibration method in CASA to improve the dynamic range of the map. The angular resolutions using “natural weighting” and “uniform

weighting” are  $0''.14 \times 0''.13$ ,  $PA = 82.5^\circ$  and  $0''.101 \times 0''.090$ ,  $PA = 3.8^\circ$ , respectively. The sensitivities are  $1\sigma = 0.10$  and  $0.18 \text{ mJy beam}^{-1}$  in the emission-free areas, respectively. The dynamic ranges are  $\sim 28000$  and  $\sim 16000$ , respectively. They are several times worse than the expected values by the ALMA sensitivity calculator. We will present the improvement of the analysis and the full results in another paper (Tsuboi et al. 2017b).

## 2.2. $H30\alpha$ recombination line

We analyzed the DDT observation toward the Galactic Center with ALMA, which was released in the autumn of 2016 (Project code: 2015.A.00021.S). The data set contains two-days observations (12/13 July 2016 and 18/19 July 2016) of the Galactic Center in the  $H30\alpha$  recombination line ( $\nu_{rest} = 231.9 \text{ GHz}$ ). The FOV is  $25''$ , which is centered at Sgr A\*. Since the original observations aimed for the measurement of the time variation of Sgr A\*, the time spans of the observations are 22:40UT - 03:40UT for the first day and 23:00UT - 05:45UT for the second day, providing good uv coverages for imaging. J1744-3116 was used as a phase calibrator. The flux density scale was determined using Titan and J1733-1304. Before spectral line imaging, the continuum emissions of Sgr A\* and the GCMS were subtracted from the data using CASA task, `mstransform (fitorder=1)` for each day of the observations. Imaging for the combined data for the two-day observations was done using CASA 5.0 with `tclean` task to use a new auto-boxing capability. We used the multi-threshold auto-boxing algorithm (`usemask='auto-multithresh'`) to automatically identify the emission regions to be CLEANed using threshold based on rms noise and sidelobe level and update as the deconvolution iterations progress<sup>1</sup>. For the weighting scheme, Briggs weighting with a robust parameter of 0.5 was used. As a result, we obtained an  $H30\alpha$  recombination line data cube with high angular resolution ( $0''.41 \times 0''.30$ ,  $PA = -77^\circ$ ) and high sensitivity ( $0.2 \text{ mJy beam}^{-1}$  at a line-free channel). The sensitivity

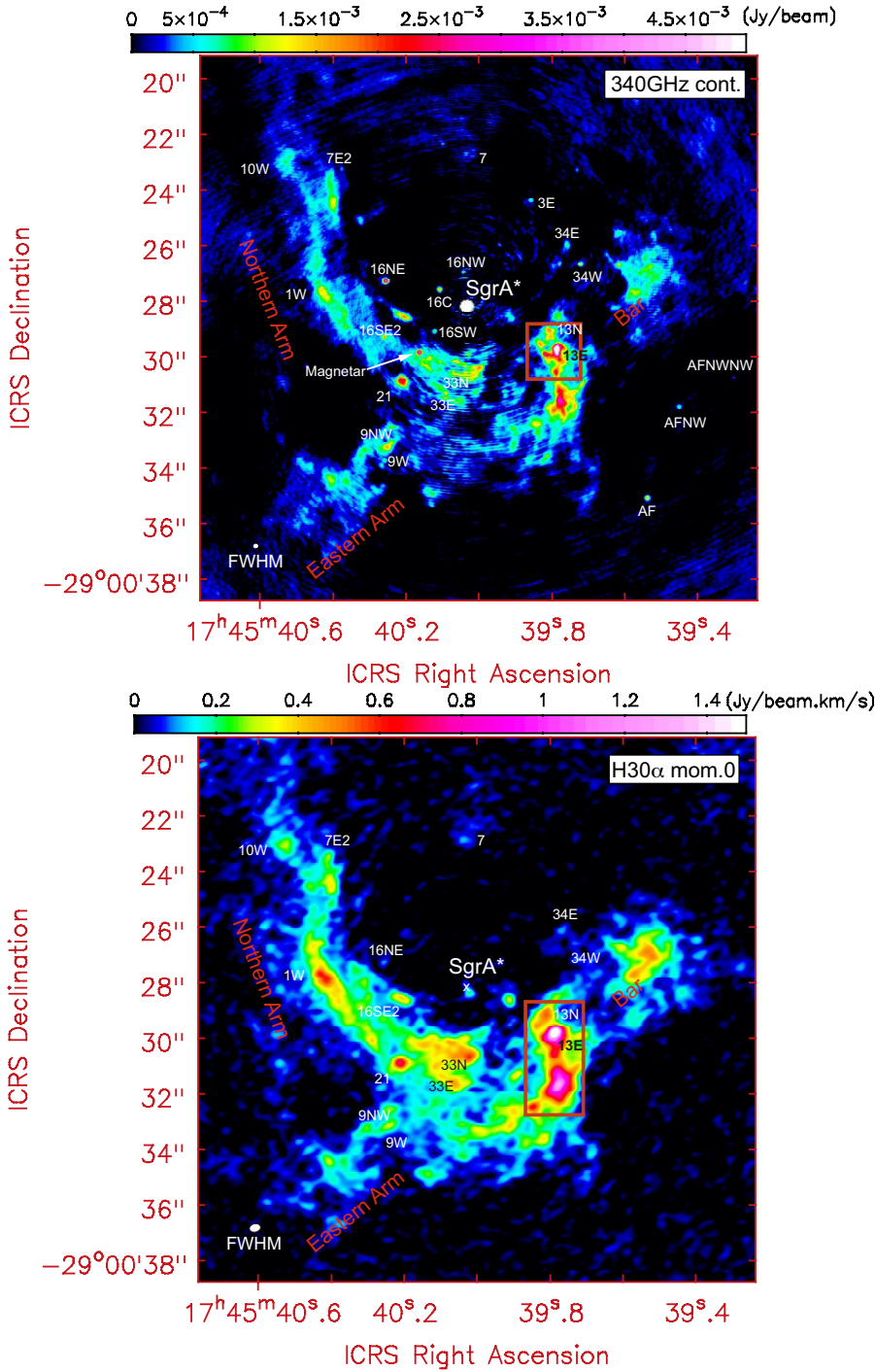
<sup>1</sup> <https://casa.nrao.edu/casadocs/casa-5.0.0/synthesis-imaging/masks-for-deconvolution>

is close to the expected one by the ALMA sensitivity calculator.

### 3. RESULTS

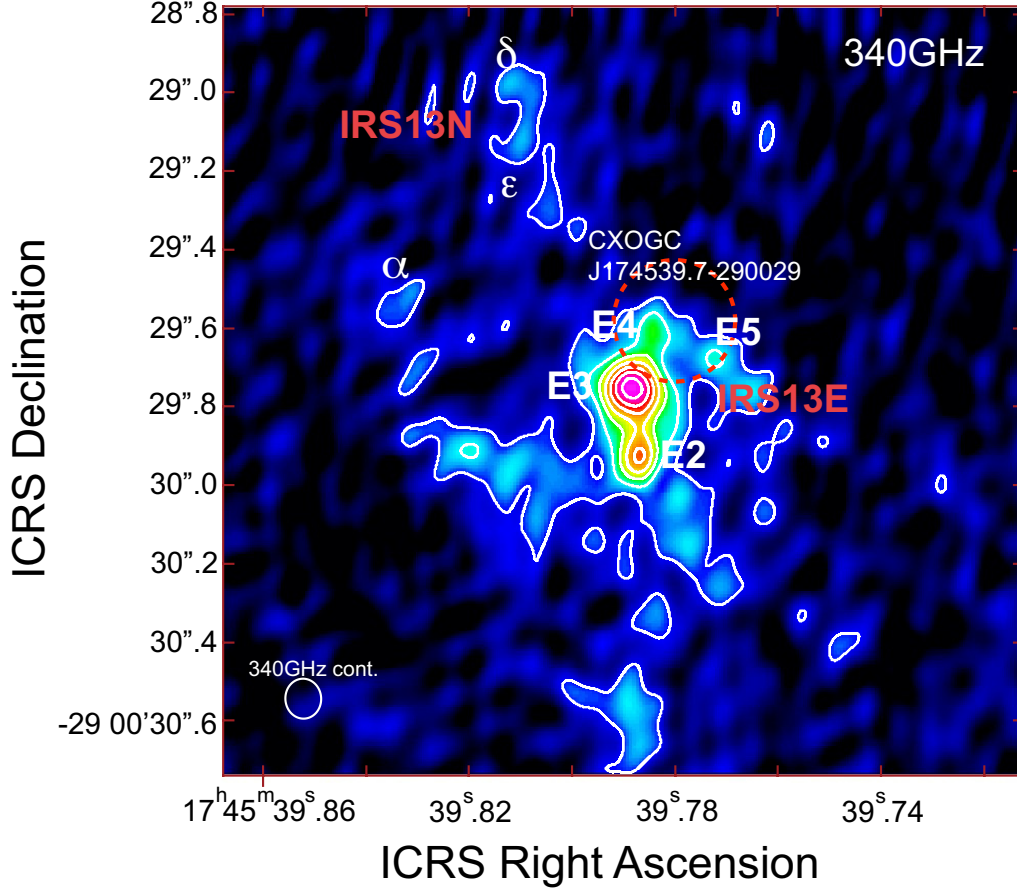
Figure 1 shows the continuum map at 340 GHz (upper panel) and the integrated intensity map of the H30 $\alpha$  recombination line with the integrated velocity range from -400 km s<sup>-1</sup> to +400 km s<sup>-1</sup> in  $V_{\text{LSR}}$  (lower panel). They are the finding charts of the structures in the GCMS (Cf. Tsuboi et al. 2016). Although the flux density of Sgr A\* was  $S_\nu = 2.8$  Jy at 340 GHz, Sgr A\* itself was not detected in the recombination line. The IRS13E complex is the most prominent both in the maps. We concentrate on the IRS13E complex in this paper although we detected several fascinating objects in these maps, for example Magnetar PSR J1745-2900 (e.g. Eatough et al. 2013) in the vicinity of Sgr A\*, which is labeled “Magnetar” in the upper panel.

Figure 2 shows the close-up continuum map of the IRS13E complex at 340 GHz. The IRS13E complex is resolved into a group of compact objects in the map. Most of these are the IR identified objects (e.g. Maillard et al. 2004; Schödel et al. 2005; Paumard et al. 2006) including IRS 13E3 which is a main member of the IRS13E complex but an ionized gas blob as noted in Introduction (Fritz et al. 2010). The positions and angular sizes of these objects are estimated by the two-dimensional Gaussian fit of CASA (see Table 1). The relative position of IRS13E3 referring to Sgr A\* is estimated to be  $\Delta\alpha = -3''.19 \pm 0''.01$ ,  $\Delta\delta = -1''.55 \pm 0''.01$ . The error is derived nominally according to ALMA Technical Handbook (10.6.6). The beam-deconvolved angular size of IRS13E3 is derived to be  $\theta_{\text{maj.obs.}} \times \theta_{\text{min.obs.}} = (0''.102 \pm 0''.008) \times (0''.090 \pm 0''.008)$ ,  $PA \sim 27^\circ$ , corresponding to the physical size of 0.0040 pc  $\times$  0.0035 pc (800 AU  $\times$  700 AU) at the Galactic center distance. The estimated size is as small as the FWHM beam size. The total flux density of IRS13E3 is  $S_{\nu 340} = 10.5 \pm 0.5$  mJy at 340 GHz by the Gaussian fit. Comparing with  $S_{\nu 42} = 13.1$  mJy at 42 GHz (Yusef-Zadeh et al. 2014), the spectrum index is estimated to be  $\alpha = \log(S_{\nu 340}/S_{\nu 42})/\log(340/42) \sim -0.1$ . The flat spectrum



**Figure 1.** The finding charts of the structures around Sgr A\* including the IRS13E complex. **Upper panel** Continuum map of Sgr A\* and the GCMS at 340 GHz in units of Jy beam<sup>-1</sup>. The FWHM beam size is  $0''.14 \times 0''.13$ ,  $PA = 82.5^\circ$  shown at the lower left corner. A red square indicates the area shown in Figure 2. **Lower panel** Integrated intensity (moment 0) map of the H30α recombination line with the integrated velocity range from  $V_{\text{LSR}} = -400$  to  $+400$  km s<sup>-1</sup> in units of Jy beam<sup>-1</sup> km s<sup>-1</sup>. The FWHM beam size is  $0''.41 \times 0''.30$ ,  $PA = -77^\circ$  shown at the lower left corner. Sgr A\* itself (cross) was not detected in the recombination line. A red rectangle indicates the area shown in Figure 3.





**Figure 2.** 340 GHz continuum emission map of the IRS13E complex with ALMA (red square in Figure 1-upper panel). The FWHM beam size is  $0''.101 \times 0''.090$ ,  $PA = 3.8^\circ$ , which is shown as the white ellipse at the lower left corner. The contour levels are 0.8, 1.6, 2.4, 3.2, 4.0, 4.8, and 5.6 mJy beam $^{-1}$  and the  $1\sigma$  noise level is 0.18 mJy beam $^{-1}$ . The red broken circle shows the position of the X-ray object: CXOGCJ174539.7-290029 ( $\alpha_{\text{ICRS}} = 17^{\text{h}}45^{\text{m}}39^{\text{s}}.780$ ,  $\delta_{\text{ICRS}} = -29^\circ00'29''.59$ ) (e.g. [Baganoff et al. 2003](#); [Muno et al. 2009](#)). The radius is the statistical error,  $0''.16$ . The IRS13N complex is also seen  $0''.5$  northeast of the IRS13E complex. The Greek symbols show the members of the IRS13N complex.

suggests that the emission from IRS13E3 is an optically thin free-free emission and the sign of dust thermal emission is not clear. The derived parameters of the IR objects are also summarized in table 1. Note that our derived values are similar to those in the previous observations (e.g. [Yusef-Zadeh et al. 2014](#); [Paumard et al. 2006](#)).

Figure 3 shows the channel maps of the IRS13E complex in the H30 $\alpha$  recombination line with the central velocities of  $V_{\text{c,LSR}} = -390$  to  $+310$  km s $^{-1}$  (the map area corresponds to the red rectangle



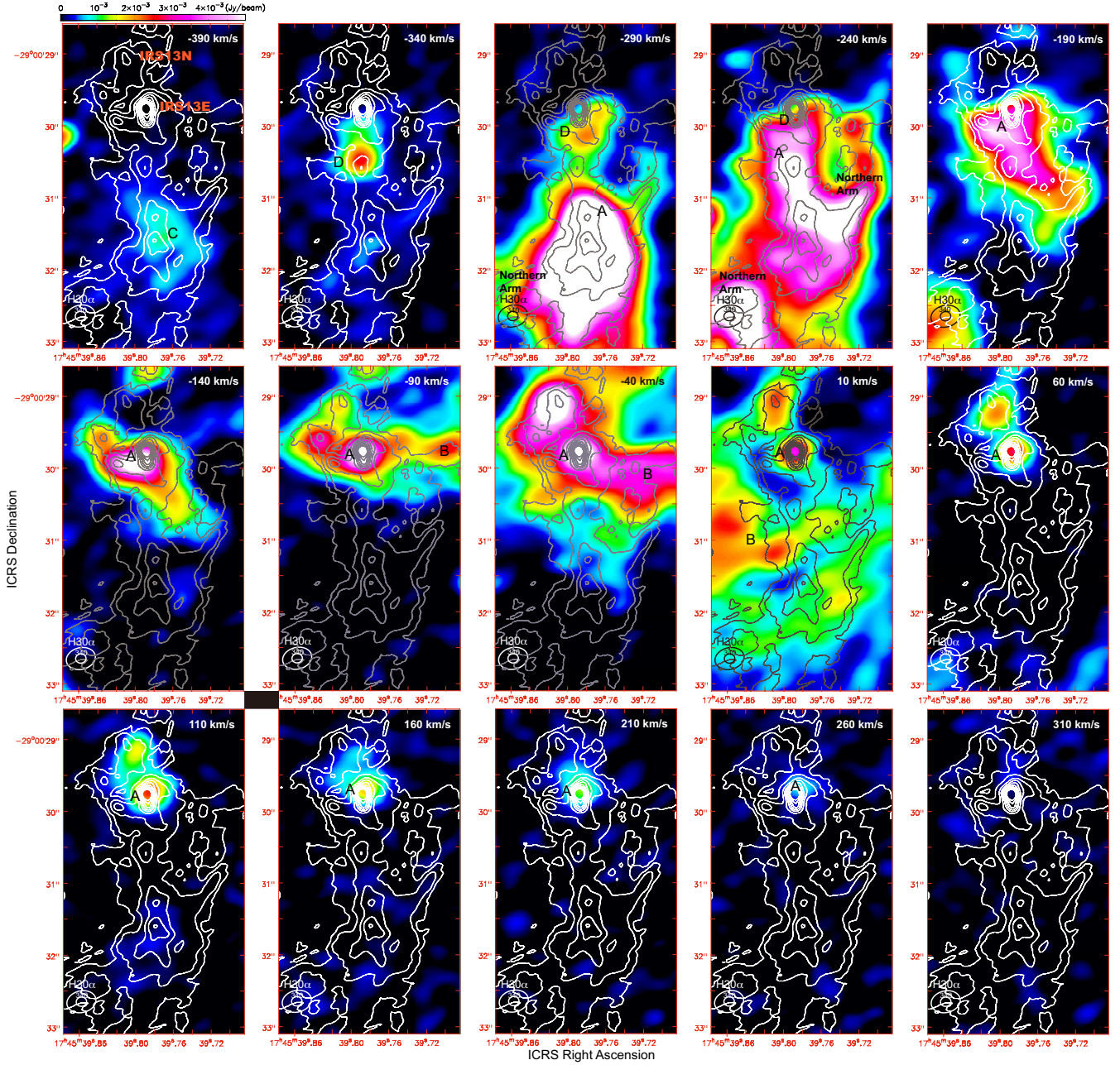


**Figure 3.** Channel maps of the IRS13E complex in the  $H30\alpha$  recombination line from  $-415 \text{ km s}^{-1}$  to  $+335 \text{ km s}^{-1}$  in  $V_{\text{LSR}}$  (red rectangle in Figure 1-lower panel). The velocity width of each panel is  $50 \text{ km s}^{-1}$ . The central velocity and the FWHM beam size,  $0''.41 \times 0''.30$ ,  $PA = -74^\circ$ , are shown at the upper right and lower left corners of each panel, respectively. The 340 GHz continuum emission is also shown as contours for comparison. The FWHM beam size,  $0''.14 \times 0''.13$ ,  $PA = 82.5^\circ$ , at 340 GHz is also shown at the lower left corner of each panel. The contour levels are 0.4, 0.8, 1.6, 2.4, 3.2, 4.0, 4.8, 5.6, and  $6.4 \text{ mJy beam}^{-1}$ . The capitals show the components shown in figure 4.

**Table 1.** Parameters of the compact objects in the IRS13E complex at 340 GHz.

Name	$\Delta\alpha^1$	$\Delta\delta^1$	$\theta_{\text{maj.}} \times \theta_{\text{min.}}^2$	$S_\nu(\text{peak})^3$	$S_\nu(\text{total})^3$	Sp. <sup>4</sup>
	[ $''$ ]	[ $''$ ]	[mas $\times$ mas, $PA$ ]	[mJy beam $^{-1}$ ]	[mJy beam $^{-1}$ ]	
Sgr A*	0.00	0.00	point source	$2807 \pm 2^5$	$2811 \pm 3^5$	–
IRS13E2	$-3.21 \pm 0.02^6$	$-1.70 \pm 0.02$	point source	$3.1 \pm 0.3$	$5.0 \pm 0.6$	WN9
IRS13E3	$-3.19 \pm 0.01$	$-1.55 \pm 0.01$	$102 \times 90, 27^\circ$	$5.4 \pm 0.2$	$10.5 \pm 0.5$	Ionized Gas
IRS13E4	$-3.24 \pm 0.02$	$-1.42 \pm 0.02$	$97 \times 77, 176^\circ$	$2.0 \pm 0.2$	$3.6 \pm 0.5$	WC9
IRS13E5	$-3.40 \pm 0.04$	$-1.47 \pm 0.04$	point source	$1.1 \pm 0.1$	$1.1 \pm 0.2$	Ionized Gas

<sup>1</sup> Peak position referring to Sgr A\* estimated by the two-dimensional Gaussian fit of CASA. The position of Sgr A\* is assumed to be  $\alpha_{\text{ICRS}} = 17^{\text{h}}45^{\text{m}}40^{\text{s}}.04$  and  $\delta_{\text{ICRS}} = -29^\circ00'28''.20$ . <sup>2</sup> Beam-deconvolved size. <sup>3</sup> Flux estimated by the two-dimensional Gaussian fit of CASA. <sup>4</sup> IR spectral type (Fritz et al. 2010). <sup>5</sup> Because Sgr A\* is a variable source, these are averages at Aug. and Sep. 2016. <sup>6</sup> The error is derived nominally according to ALMA Technical Handbook (10.6.6).

in Figure 1-lower panel). The velocity width of the channel maps is  $\Delta v = 50 \text{ km s}^{-1}$ . Figure 4a shows the integrated intensity map of the H30 $\alpha$  recombination line with the integrated velocity range of  $V_{\text{LSR}} = -400$  to  $+400 \text{ km s}^{-1}$ . These maps also show the 340 GHz continuum emission as the contours. The ionized gas seen in the panels with  $V_{\text{c,LSR}} \sim -340$  to  $+260 \text{ km s}^{-1}$  seems to be along a continuum north-south ridge including the IRS13E complex. Figure 4b shows the position velocity diagram of the H30 $\alpha$  recombination line through the IRS13E complex along the red rectangle shown in figure 4a.

There is a compact component located at  $\sim 1''$  south of IRS13E3 in the panel with  $V_{\text{c,LSR}} = -340 \text{ km s}^{-1}$  of Figure 3, which is labeled “D”. The compact component is approaching to IRS13E3 with increasing velocity (see the panels with  $V_{\text{c,LSR}} = -340, -290$ , and  $-240 \text{ km s}^{-1}$ ). This is also identified as a component in the position velocity diagram. An extended component appears around

$\sim 2''$  south of IRS13E3 in the panel with  $V_{\text{c,LSR}} = -290 \text{ km s}^{-1}$ , which is labeled “A”. The component also shifts to north with increasing velocity and reaches to IRS13E3 in the panel with  $V_{\text{c,LSR}} \sim -190 \text{ km s}^{-1}$ . The components D and A seem to be combined at IRS13E3 and the combined compact component stays here in the velocity range of  $V_{\text{c,LSR}} = -90 \text{ to } +260 \text{ km s}^{-1}$ . The peak position seems to shift monotonically to the north across the IRS13E3 in the velocity range of  $-90 \text{ to } +210 \text{ km s}^{-1}$ . The peak shift is shown clearly in Figure 4d. The behavior is also identified as a prominent curved ridge with a wide velocity width in Figure 4b. The negative angular offset part of the curved ridge corresponds to the south extended component in the panels with  $V_{\text{c,LSR}} \sim -290 \text{ to } -190 \text{ km s}^{-1}$  of Figure 3. The velocity width of the ionized gas toward IRS13E3 reaches to  $\Delta v_{\text{FWZI}} \sim 650 \text{ km s}^{-1}$  (Full Width at Zero Intensity; FWZI) at IRS13E3.

A nearly vertical ridge with  $V_{\text{LSR}} \sim -50 \text{ to } +50 \text{ km s}^{-1}$  is identified in the position velocity diagram of Figure 4b, which is labeled “B”. This corresponds to an extended component surrounding the IRS13E and IRS13N complexes seen in the channel map of  $V_{\text{c,LSR}} = -90 \text{ to } 10 \text{ km s}^{-1}$  of Figure 3. The component is a part of the Bar which is a substructure of the GCMS (also see Figure 1). The ionized gas probably associated with the IRS13N complex is also identified in the panels with  $V_{\text{c,LSR}} \sim -90 \text{ to } +110 \text{ km s}^{-1}$  of Figure 3.

In addition, a faint ridge is seen in the position velocity diagram of Figure 4b, which is labeled “C”. The component is the counterpart in the  $\text{He30}\alpha$  recombination line of the negative velocity vertical part of the components “A” because the velocity shift is exactly equal to the velocity difference between the  $\text{H30}\alpha$  and  $\text{He30}\alpha$  recombination lines;  $\Delta v = c[\nu(\text{He30}\alpha) - \nu(\text{H30}\alpha)]/\nu(\text{H30}\alpha) \sim -122 \text{ km s}^{-1}$ . This component is also identified as a faint extended component  $\sim 2''$  south of IRS13E3 in the channel map of  $V_{\text{c,LSR}} \sim -390 \text{ km s}^{-1}$  (see Figure 3). The intensity ratio of  $\frac{I(\text{He30}\alpha)}{I(\text{H30}\alpha)}$  has a reasonable value of  $\sim 0.05$  in galactic disk HII regions (e.g. [Roshi, Churchwell, & Anderson 2017](#)).

Figure 4c shows the position velocity diagram of the  $\text{H30}\alpha$  recombination line along the cut adjacent

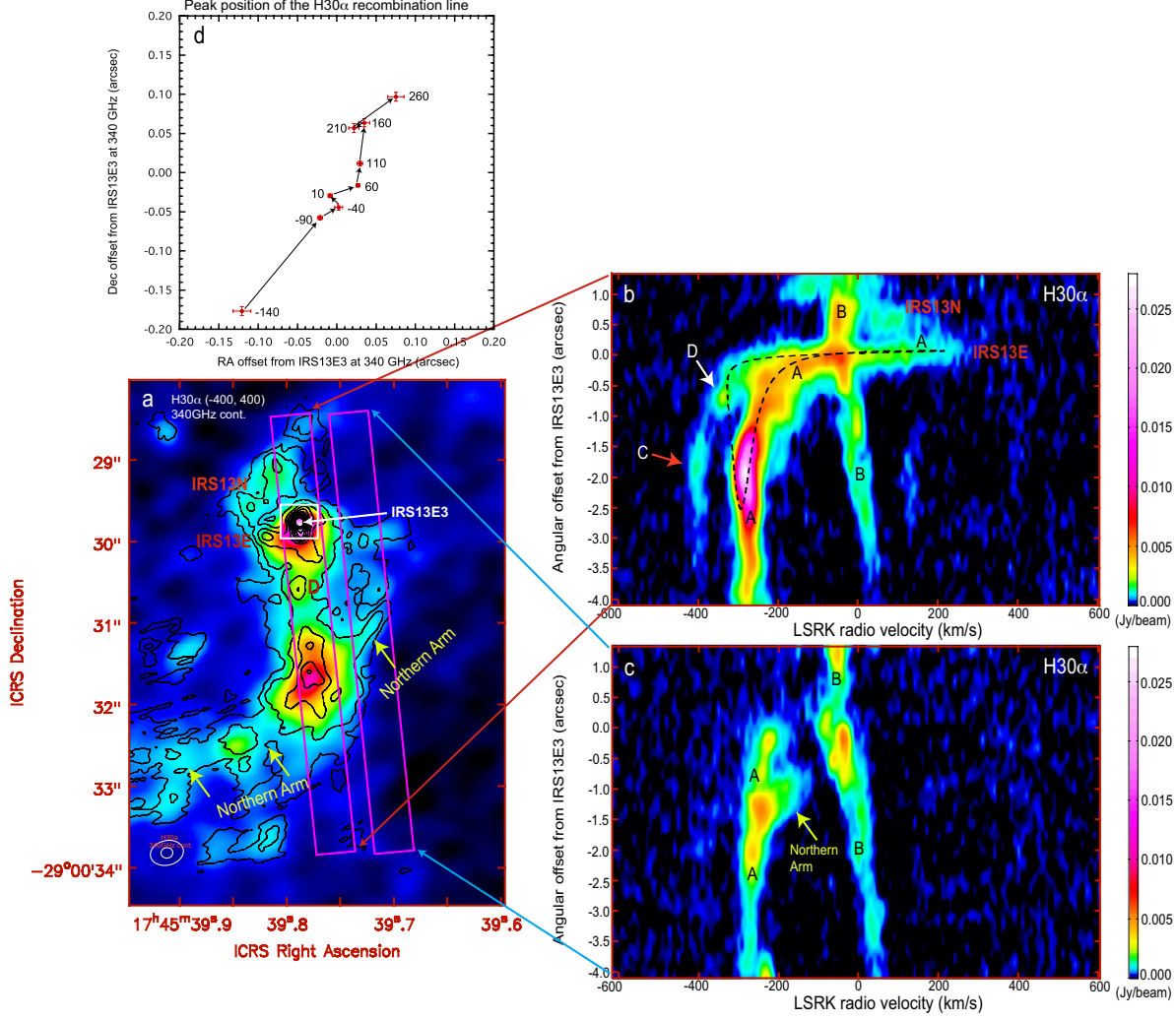


**Figure 4.** **a** Integrated intensity map of the H30 $\alpha$  recombination line with the integrated velocity range of  $V_{\text{LSR}} = -400$  to  $+400$  km s $^{-1}$ . The contours show the 340 GHz continuum emission with ALMA. The FWHM beam sizes are shown as white ovals at the lower left corner. The red rectangle shows the cutting area of the position-velocity diagram of panel **b**. The white square shows the area of panel **c**. Yellow arrows show the tip of the Northern Arm (NA) of the Minispirals. **b** Position velocity diagram of the H30 $\alpha$  recombination line through the IRS13E complex along the cutting area shown in the panel **a** in units of Jy beam $^{-1}$ . There is a curved ridge with a wide velocity width (“A”), which reaches to  $\Delta v_{\text{FWZI}} \sim 650$  km s $^{-1}$  (Full Width at Zero Intensity; FWZI) at IRS13E3, and a relatively narrow velocity width component around  $V_{\text{LSR}} \sim -50$  to  $+50$  km s $^{-1}$  (“B”). A black broken line shows an example of the Keplerian orbits that describe well the observed features. The eccentricity, the semi-major axis, and the position angle are  $e \sim 0.97$ ,  $a \sim 1.4 \times 10^{17}$  cm, and  $PA \sim 60^\circ$ , respectively. **c** Position velocity diagram of the H30 $\alpha$  recombination line adjacent parallel to **b**. Yellow arrow shows the tip of the NA. **d** Peak positions of the H30 $\alpha$  recombination line derived by 2-D Gaussian fit. Numbers show the  $V_{\text{c,LSR}}$ .

and parallel to the cut for Figure 4b for comparison. This indicates the relations between the ionized gas associating with the IRS13E complex and the arms of the GCMS. The tip of the Eastern Arm (EA) is located around  $\alpha_{\text{ICRS}} = 17^{\text{h}}45^{\text{m}}40^{\text{s}}.03$ ,  $\delta_{\text{ICRS}} = -29^{\circ}00'30''.5$  (see the lower panel of Figure 1), which is far from the ionized gas associating with the IRS13E complex. Therefore, there is no connection with the EA and the ionized gas. The ionized gas is independent from the EA. On the other hand, the relation between the ionized gas and the Northern Arm (NA) is complicated. The tip of the NA crosses the ionized gas around  $2''$  south of IRS13E as shown in Figure 4a (yellow arrows, see also the panels with  $V_{\text{c,LSR}} \sim -290$  to  $-190$  km s $^{-1}$  of Figure 3). Although the tip of the NA is partially blended with the ionized gas, this is barely identified in the position velocity diagram of Figure 4c (yellow arrow). The ionized gas would be independent from the NA.

## 4. DISCUSSION

### 4.1. Compactness of the Ionized Gas toward IRS13E3

The angular source size of the ionized gas toward IRS13E3 is derived to be  $\theta_{\text{maj.obs.}} \times \theta_{\text{min.obs.}} = 0''.41 \pm 0''.03 \times 0''.31 \pm 0''.02$ ,  $PA \sim 127^{\circ}$  by the two-dimensional Gaussian fit to the total integrated velocity map (see Figure 1-lower panel). Because this is as large as the clean beam size of the H30 $\alpha$  recombination line, the beam-deconvolved source size is estimated to be much less than the beam size. The peak position is also estimated to be  $\alpha_{\text{ICRS}} = 17^{\text{h}}45^{\text{m}}39^{\text{s}}.785 \pm 0''.001$ ,  $\delta_{\text{ICRS}} = -29^{\circ}00'29''.84 \pm 0''.01$ . This position is almost equal to that of IRS13E3 in the 340 GHz continuum map within the FWHM beam size. The positional differences are  $\Delta\alpha \sim 0''.005$  and  $\Delta\delta \sim 0''.028$  according to the comparison between the 340 GHz continuum and H30 $\alpha$  moment 0 positions of IRS16NE, of which images are compact both in the maps (see Figure 1). The positional correspondence between both the observation is better than 10% of the FWHM beam size of the H30 $\alpha$  moment 0 map ( $\sim 0''.4$ ).

Because IRS13E3 is emitting the 340 GHz continuum through thin free-free emission mechanism



as mentioned above, IRS13E3 is emitting the H30 $\alpha$  recombination line simultaneously. The area emitting the recombination line should be identical to IRS13E3 itself shown in the continuum map (see Figure 2). The size of the ionized gas would be  $\theta_{\text{maj.obs.}} \times \theta_{\text{min.obs.}} = 0''.102 \times 0''.090$ ,  $PA \sim 27^\circ$  or  $r_{\text{maj}} \times r_{\text{min.obs.}} = 0.0020 \text{ pc} \times 0.0018 \text{ pc}$  (400 AU  $\times$  350 AU). Although our estimated radius,  $r$ , is an upper limit, this radius is considered to be close to the real radius because the continuum observation of IRS13E3 with JVL A at 34 GHz shows a similar source size;  $0''.08 \times 0''.04$  (Yusef-Zadeh et al. 2014). The compactness and large velocity width suggest the presence of an IMBH in the IRS13E complex.

#### 4.2. Keplerian Orbit with High Eccentricity around IRS13E3?

There is a bright ridge connecting IRS13E3 with the extended component around  $\sim 2''$  south of IRS13E3 in Figure 4a. This corresponds to the curved ridge from  $V_{\text{LSR}} \sim -300$  to  $+250 \text{ km s}^{-1}$  (“A”) in the position velocity diagram of figure 4b. In addition, there is also a weak component at  $V_{\text{LSR}} \sim -350 \text{ km s}^{-1}$  at the offset of  $\sim -0''.5$  (“D”; white arrow) in the position velocity diagram. The weak component is identified as a compact component at  $0''.8$  south IRS13E3 in the channel map of  $V_{\text{c,LSR}} = -340 \text{ km s}^{-1}$  as mentioned in the previous section (see Figure 3). These observed features suggest the presence of a Keplerian orbit with high eccentricity around IRS13E3. Such Keplerian orbits have a nearly linear part with large velocity gradient and double curved ridges with relatively small velocity gradient in the position velocity diagram (see Figure 12 in Tsuboi et al. 2017). In the case, the line intensity on the orbit decreases with increasing velocity as shown in Figure 4b because the line intensity should be in inverse proportion to the orbital velocity. Note that the thermal velocity broadening for ionized Hydrogen gas of  $10^4 \text{ K}$  is  $\Delta v \sim 20 \text{ km s}^{-1}$  in FWHM, which is negligible as compared with the rotation velocity.

Another hypothesis to explain the weak component D may be that the component is the counterpart in the He30 $\alpha$  recombination line. However, the intensity ratio of the bright ridge and weak component

is up to  $\sim 0.3$ . This is too high as  $\frac{I(\text{He30}\alpha)}{I(\text{H30}\alpha)}$ . In addition, the velocity shift between these components is  $\Delta v \sim -100 \text{ km s}^{-1}$  which is less than the velocity difference between the H30 $\alpha$  and He30 $\alpha$  recombination lines,  $\Delta v \sim -122 \text{ km s}^{-1}$ , as mentioned previously. Therefore, the weak component would be a part of the Keplerian orbit with a high eccentricity around IRS13E3.

An example of the orbits describing well the observed features is shown in the position velocity diagram (see the black broken line in Figure 4b). Note that it is difficult to determine exclusively the accurate orbital parameters by fitting in the position velocity diagram because the full orbit is not completely occupied by ionized gas and/or the observed features are not always belong to a single orbit. The apoastron of the orbit would be located in the bright extended ionized gas component seen  $\sim 2''$  south of the IRS13E complex in projection. The angle between the direction of the semi-major axis and the line of sight is  $PA \sim 60^\circ$ . The observed major axis is  $2a \sin 60^\circ \sim 2.5 \times 10^{17} \text{ cm}$ . Then the semi-major axis of the orbit is estimated to be  $a \sim 1.4 \times 10^{17} \text{ cm} = 1 \times 10^4 \text{ AU}$ . The inclination angle of the orbit would be  $i \sim 0^\circ$  because of the elongated feature with a narrow width of the orbiting ionized gas shown in Figure 4a. By the comparison between the observed shape in the position velocity diagram and the calculated Keplerian orbits, the eccentricity of the orbit is estimated to be  $e \sim 0.97$ .

#### 4.3. The Enclosed Mass of IRS13E3

The presence of an IMBH in the IRS13E complex is strongly supported by a large enclosed mass of IRS13E3. In the case of nearly edge-on view, the velocity width of the Keplerian orbit is estimated by

$$\Delta V \sim \left( \sqrt{\frac{1+e}{1-e}} + \sqrt{\frac{1-e}{1+e}} \right) \sqrt{\frac{GM}{a}}. \quad (1)$$

Then the enclosed mass is estimated to be

$$M \sim a \Delta V^2 \left( \sqrt{\frac{1+e}{1-e}} + \sqrt{\frac{1-e}{1+e}} \right)^{-2} G^{-1}. \quad (2)$$



The observed velocity width is  $\Delta V \sim 600 \text{ km s}^{-1}$ , and the enclosed mass of the object is estimated to be  $M \sim 4 - 7 \times 10^4 M_\odot$ , comparable to the mass of an IMBH, for  $e = 0.96 - 0.98$  and  $a \sim 1.4 \times 10^{17} \text{ cm}$ . Although the Keplerian orbit has large ambiguities in the orbit parameters, the mass would be consistent with  $M \sim 10^4 M_\odot$  in the IRS13E complex (e.g. [Maillard et al. 2004](#); [Schödel et al. 2005](#); [Paumard et al. 2006](#)). Even in the case that the compact ionized gas is not belong to the Keplerian orbit, the compactness and large velocity width would indicate  $\sim 10^4 M_\odot$  in the IRS13E complex.

If there is an IMBH orbiting around Sgr A\*, the position of Sgr A\* must be affected by it. The position of Sgr A\* on the celestial sphere has been monitored using VLBA for a long time over 15 years (e.g. [Reid&Brunthaler 2004](#)). The positional shift along the Galactic plane is as large as  $-6.4 \text{ mas year}^{-1}$ . However, one can not distinguish between the perturbation by the massive object and the proper motion by the Galactic rotation. On the other hand, the positional shift crossing the Galactic plane is found to be as small as  $-0.2 \text{ mas year}^{-1}$ . This indicates that the upper limit mass of the second black hole is  $M \lesssim 10^4 M_\odot$  in the area of  $r \sim 10^3 - 10^5 \text{ AU}$  from Sgr A\* ([Reid&Brunthaler 2004](#)). Therefore, there is no conflict between our derived enclosed mass and the upper limit mass of the second black hole inferred from the VLBA observations.

The periastron distance is estimated to be  $a(1 - e) = 4.3 \times 10^{15} \text{ cm}$  and the projected distance from Sgr A\* is  $r_{\text{proj.}} \sim 4 \times 10^{17} \text{ cm}$ . Because the mass of the IMBH is only 1% of the mass of Sgr A\*, the gravity of the IMBH associated with IRS13E3 is comparable to that of Sgr A\* even around the periastron of the Keplerian orbit around IRS13E3. However, the flow of the ionized gas, which is extended to south, seems to be described by a Keplerian orbit as mentioned above. This means that the gravity of the IMBH would be dominant there, and the IMBH might be located fairly far from Sgr A\* than the projected distance.

The ionized gas mass on the orbit is estimated to be  $M \sim 6 \times 10^{-3} M_\odot$  based on this observation assuming the electron temperature of  $T_e \sim 1 \times 10^4 \text{ K}$  and the electron density of  $n_e \sim 1 \times 10^6 \text{ cm}^{-3}$

(e.g. [Murchikova 2017](#); [Tsuboi et al. 2017](#)). When all the ionized gas falls to the IMBH associated with IRS13E3 within one orbital period;  $T = 2\pi\sqrt{\frac{a^3}{GM}} \sim 4 \times 10^3$  yr, the upper limit of the mass accretion rate is estimated to be  $M/T \lesssim 1 \times 10^{-6} M_{\odot} \text{ yr}^{-1}$ . However, because both approaching gas to IRS13E3 (probably D) and going-away gas (probably A) are observed on the orbit (Cf. [Oka et al. 2016](#)), it would be overestimation that all gas falls into it within an orbital period. If the efficiency of the accretion is assumed to be 1 % as a likely value, the mass accretion rate becomes comparable to the mass accretion rate of Sgr A\* (e.g. [Quataert & Gruzinov 2000](#); [Genzel et al. 2010](#)).

#### 4.4. X-ray Counterpart of IRS13E3?

Figure 2 also shows the position of a discrete X-ray source detected in the IRS 13E complex, CXOGCJ174539.7-290029 ( $\alpha_{\text{ICRS}} = 17^{\text{h}}45^{\text{m}}39^{\text{s}}.780$ ,  $\delta_{\text{ICRS}} = -29^{\circ}00'29''.59$ ) (e.g. [Baganoff et al. 2003](#); [Muno et al. 2009](#)). The statistical error and absolute uncertainty of the position are  $0''.16$  and  $0''.76$  in radius, respectively ([Baganoff et al. 2003](#)). The X-ray source is located near the 340-GHz continuum peak position of IRS13E3 with a positional difference of  $\sim 0''.2$  (see Table 1), which is smaller than the uncertainty of the X-ray observation. Such a small positional difference is generally caused by using different reference frames. Therefore, we consider that the two positions are coincident. In addition, in the case that the compact component is a part of the ionized gas orbiting around the periastron as shown previously, it is possible that the component and the X-ray source corresponding to the IMBH are observed to be up to the periastron distance apart ( $\sim 0''.3$ ).

The X-ray photon flux is  $F_{2-8\text{keV}} = 3.092 \times 10^{-7} \text{ cm}^{-2} \text{ s}^{-1}$  at 1999.72 yr, which is a half of that of Sgr A\* (e.g. [Muno et al. 2009](#)). The spectrum of this bright X-ray source resembles that of the quiescent emission from the hot plasma around Sgr A\* and the source has no long- and short-timescale variabilities ([Muno et al. 2009](#)). The X-ray emission should be originated by the hot plasma located at IRS13E3 through bremsstrahlung rather than those from usual X-ray binaries,

cataclysmic variables, and so on. Thus we consider that this source is the X-ray counterpart of IRS13E3. The large X-ray photon flux may be consistent with the mass accretion rate estimated in the previous subsection.

## 5. CONCLUSIONS

We detected the ionized gas associated with IRS13E3 in the  $H30\alpha$  recombination line using ALMA, which has a wide velocity width ( $\Delta v_{\text{FWZI}} \sim 650 \text{ km s}^{-1}$ ) and compactness ( $r \sim 0.002 \text{ pc}=400 \text{ AU}$ ). The enclosed mass is estimated to be  $10^4 M_{\odot}$  in the case of the Keplerian orbit with high eccentricity around IRS13E3. The mass does not conflict with the upper limit mass of the IMBH around Sgr A\* which is derived by the long-term astrometry with VLBA. This object presumably has an X-ray counterpart. Consequently, a very fascinating possibility is that the detected ionized gas is orbiting around an IMBH with  $10^4 M_{\odot}$  embedded in the IRS13E complex.

This work is supported in part by the Grant-in-Aid from the Ministry of Education, Sports, Science and Technology (MEXT) of Japan, No.16K05308. The National Radio Astronomy Observatory is a facility of the National Science Foundation operated under cooperative agreement by Associated Universities, Inc. USA. This paper makes use of the following ALMA data: ADS/JAO.ALMA#2015.1.01080.S and ALMA#2015.A.00021.S. ALMA is a partnership of ESO (representing its member states), NSF (USA) and NINS (Japan), together with NRC (Canada), NSC and ASIAA (Taiwan), and KASI (Republic of Korea), in cooperation with the Republic of Chile. The Joint ALMA Observatory is operated by ESO, AUI/NRAO and NAOJ.

*Facilities:* ALMA

## Software: CASA

## REFERENCES

- Baganoff, F. K. et al. 2003, *ApJ*, 591, 891
- Boehle, A. et al. 2016, *ApJ*, 830, 17
- Eatough, R. P., et al. 2013, *Nature*, 501, 391
- Ekers, R. D., van Gorkom, J. H., Schwarz, U. J., & Goss, W. M., 1983, *A&A*, 122, 143
- Fritz, T. K et al., 2010, *ApJ*, 721, 395
- Genzel, R., Thatte, N., Krabbe, A., Kroker, H., & Tacconi-Garman, L. E. 1996, *ApJ*, 472, 153
- Genzel, R., Eisenhauer, F., & Stefan Gillessen, S. 2010, *Rev. Mod. Phys.*, 82, 3121
- Gerhard, O., 2001, *ApJL*, 546, L39
- Ghez, A. M., et al. 2008, *ApJ*, 689, 1044
- Gillessen, S., Eisenhauer, F., Trippe, S., Alexander, T., Genzel, R., Martins, F., & Ott, T. 2009, *ApJ*, 692, 1075
- Lacy, J. H., Townes, C. H., Geballe, T. R., & Hollenbach, D. J. 1980, *ApJ*, 241, 132
- Lo, K.Y. & Claussen, M. J., 1983, *Nature*, 306, 647
- Maillard, J. P.; Paumard, T.; Stolovy, S. R.; Rigaut, F. 2004, *A&A*, 423, 155
- McMullin, J. P., Waters, B., Schiebel, D., Young, W., & Golap, K. 2007, *Astronomical Data Analysis Software and Systems XVI* (ASP Conf. Ser. 376), ed. R. A. Shaw, F. Hill, & D. J. Bell (San Francisco, CA: ASP), 127
- Muno, M.P. et al. 2009, *ApJS*, 181, 110
- Murchikova, E. 2017, in *Proc. IAU Symp.* 322, The Multi-Messenger Astrophysics of the Galactic Centre, ed. R. C. Crocker, S. N. Longmore, & G.V. Bicknell, 21
- Quataert, E. & Gruzinov, A., 2000, *ApJ*, 542, 842
- Öka, T., Mizuno, R., Miura, K., & Takekawa, S. 2016, *ApJ*, 816, id.L7
- Paumard, T., et al. 2006, *ApJ*, 643, 1011
- Reid, M. J. & Brunthaler, A. 2004, *ApJ*, 616, 872
- Roshi, D. A., Churchwell, E. & Anderson, L. D., 2017, *ApJ*, 838, 144
- Schödel, R., Eckart, A., Iserlohe, C., Genzel, R., & Ott, T., 2005, *ApJL*, 625, L111
- Schödel, R., Merritt, D. & Eckart, A., 2009, *A&A*, 502, 91
- Tsuboi, M., Kitamura, Y., Miyoshi, M., Uehara, K., Tsutsumi, T., & Miyazaki, A., 2016, *PASJ*, 68, id. L7
- Tsuboi, M., Kitamura, Y., Uehara, K., Miyawaki, R., Tsutsumi, T., Miyazaki, A., & Miyoshi, M., 2017, *ApJ*, 824, id. 94
- Tsuboi, M., Kitamura, Y., Miyoshi, M., Uehara, K., Tsutsumi, T., Miyawaki, R., & Miyazaki, A., 2017, in preparation.
- Yusef-Zadeh, F., Roberts, D. A., Bushouse, H., Wardle, M., Cotton, W., Royster, M., & van Moorsel, G. 2014, *ApJL*, 792, L1